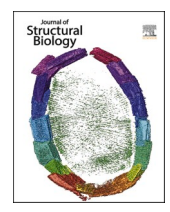
ELSEVIER

Contents lists available at ScienceDirect

# Journal of Structural Biology

journal homepage: www.elsevier.com/locate/yjsbi



# Solid-state NMR MAS CryoProbe enables structural studies of human blood protein vitronectin bound to hydroxyapatite



T. Gopinath <sup>a</sup>, Kyungsoo Shin <sup>a</sup>, Ye Tian <sup>a</sup>, Wonpil Im <sup>b</sup>, Jochem Struppe <sup>c</sup>, Barbara Perrone <sup>d</sup>, Alia Hassan <sup>d</sup>, Francesca M. Marassi <sup>a</sup>, <sup>\*</sup>

- <sup>a</sup> Department of Biophysics, Medical College of Wisconsin, Milwaukee, WI 53226, USA
- b Departments of Biological Sciences, Chemistry, and Bioengineering, Lehigh University, PA 18015, USA
- <sup>c</sup> Bruker Biospin Corporation, 15 Fortune Drive, Billerica, MA 01821, USA
- <sup>d</sup> Bruker Switzerland AG, Fallanden, Switzerland

### ARTICLE INFO

Edited by Benjamin Wylie

Keywords: Solid state NMR Cryo MAS Vitronectin

### ABSTRACT

The low sensitivity of nuclear magnetic resonance (NMR) is a major bottleneck for studying biomolecular structures of complex biomolecular assemblies. Cryogenically cooled probe technology overcomes the sensitivity limitations enabling NMR applications to challenging biomolecular systems. Here we describe solid-state NMR studies of the human blood protein vitronectin (Vn) bound to hydroxyapatite (HAP), the mineralized form of calcium phosphate, using a CryoProbe designed for magic angle spinning (MAS) experiments. Vn is a major blood protein that regulates many different physiological and pathological processes. The high sensitivity of the CryoProbe enabled us to acquire three-dimensional solid-state NMR spectra for sequential assignment and characterization of site-specific water-protein interactions that provide initial insights into the organization of the Vn-HAP complex. Vn associates with HAP in various pathological settings, including macular degeneration eyes and Alzheimer's disease brains. The ability to probe these assemblies at atomic detail paves the way for understanding their formation.

The ectopic deposition of lipids and proteins with mineralized calcium-phosphate is a hallmark of Age-related Macular Degeneration (AMD) and Alzheimer's Disease (AD), disorders that are currently incurable and represent the leading cause of central vision loss (van Leeuwen et al., 2003; Friedman et al., 2004) and dementia (Anon., 2022; Hurd et al., 2013) among the aging population. Biophysical studies have provided fundamental insights about mineralized deposition in AMD (Bergen et al., 2019; Thompson et al., 2015; Tan et al., 2018), AD (Tsolaki et al., 2022), atherosclerosis (Bertazzo et al., 2013), breast cancer (Tsolaki et al., 2021), and other diseases, but the process of mineralized deposition is poorly understood and it remains unclear why some deposits progress to the disease state while others do not.

Solid-state nuclear magnetic resonance (NMR) spectroscopy and cryogenic electron microscopy (cryo-EM) have played a central role in elucidating the molecular structures of amyloid fibrils observed in AD and related diseases (reviewed Tycko, 2016; Gallardo et al., 2020) but solid-state NMR is uniquely suited for structural studies of multicomponent assemblies like the mineralized deposits observed in aging pathologies. Since NMR signals are highly susceptible to the local

environment of their corresponding atomic sites, they can report on even very weak intermolecular interactions and the recent developments of *in situ* and *in cell* NMR offer new and exciting opportunities for probing biomolecular structures and interactions in native biological settings (Takahashi et al., 2013; Frederick et al., 2015; Kaplan et al., 2016; Kent et al., 2021; Luchinat et al., 2022; Theillet, 2022).

These advantages however are countered by the inherently low intensity of NMR signals over noise, which in the case of solid-state NMR is exacerbated by experiments based on detection of low sensitivity nuclei, like  $^{13}\mathrm{C}$  and  $^{15}\mathrm{N}$ , compared to the high sensitivity  $^1\mathrm{H}$  detection typical of solution NMR experiments. This fundamental sensitivity limitation often necessitates extensive signal averaging times, which can compromise sample stability and complicate signal detection from sites that undergo chemical or dynamic exchange on the millisecond time scale.

Various aspects of NMR technology have been developed to overcome this fundamental signal intensity challenge, including high-field magnets (Callon et al., 2021; Gan et al., 2017), dynamic nuclear polarization (DNP) (Chow et al., 2022; Biedenbander et al., 2022; Jaudzems et al., 2019), fast magic angle spinning (MAS) probes that enable <sup>1</sup>H

E-mail address: fmarassi@mcw.edu (F.M. Marassi).

<sup>\*</sup> Corresponding author.

detection experiments (Penzel et al., 2019), efficient multi-dimensional pulse sequences (Andreas et al., 2016; Gopinath et al., 2020), and radio frequency (RF) coil designs that avoid heating caused by high power RF pulses during decoupling (Gor'kov et al., 2007; Grant et al., 2010).

Recently, Bruker Biospin introduced a MAS solid-state NMR cryogenic probe reporting a 3–4 fold enhancement in <sup>13</sup>C and <sup>15</sup>N signal intensity over the standard room-temperature design in studies of proteins in crystalline, fibrillar and condensed liquid states, as well as pharmaceutical drugs (Gibbs et al., 2020; Hassan et al., 2020; Holmes

et al., 2022; Du et al., 2023). As in the previously developed solution NMR CryoProbe, thermal noise is reduced by cooling the RF components and preamplifiers to cryogenic temperatures, thereby enhancing signal intensity over noise, while the sample temperature is regulated independently, allowing biomolecules to be studied at physiological temperatures with high sensitivity.

Here we report MAS CryoProbe solid-state NMR studies of the human blood protein vitronectin (Vn) associated with hydroxyapatite (HAP), the major form of mineralized calcium-phosphate associated with AMD.

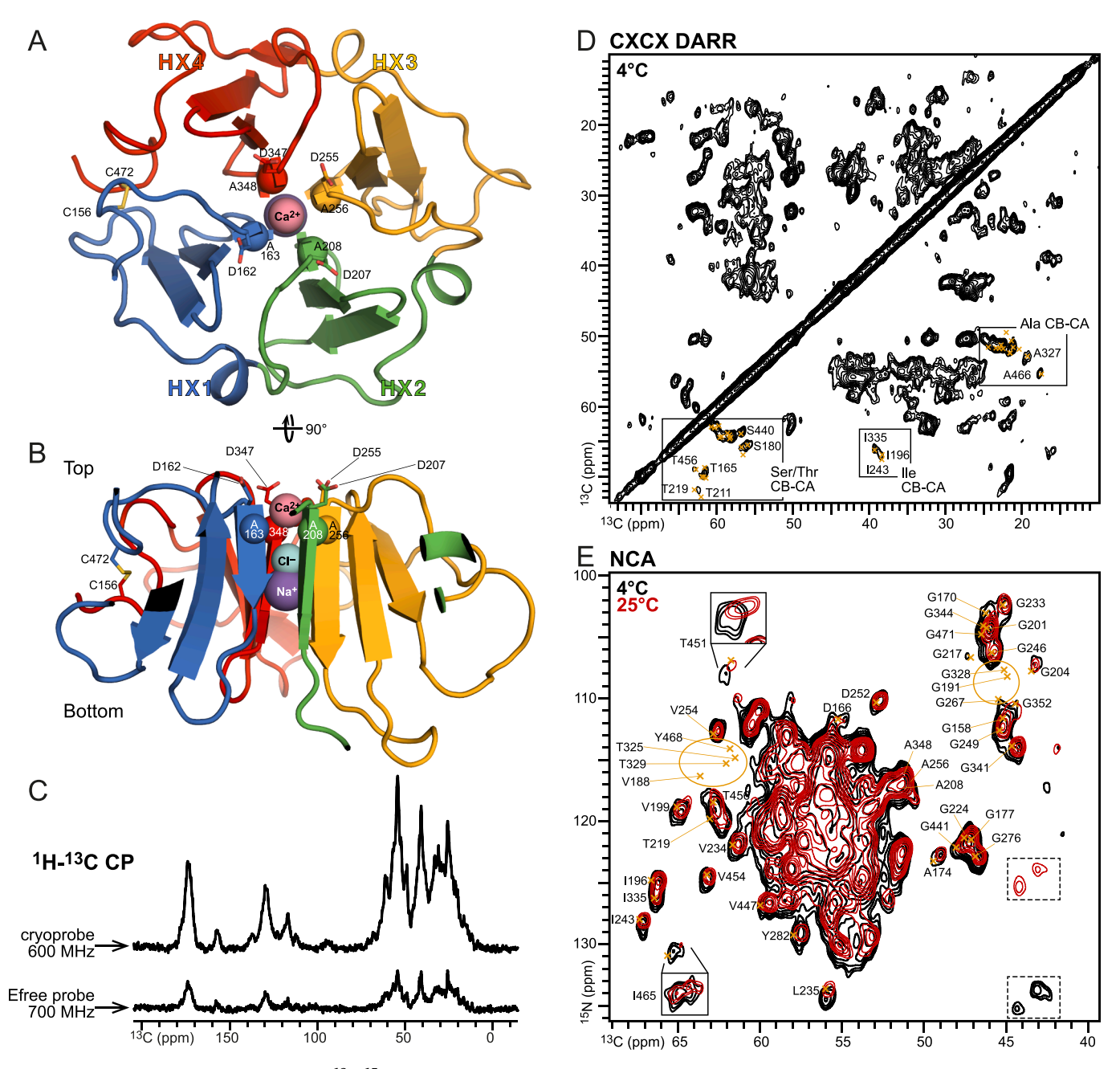


**Fig. 1. Solid-state NMR spectra of HAP-bound** <sup>13</sup>C/<sup>15</sup>N-Vn-HX. Spectra were acquired using the CryoProbe (at 14.1 T, 12 kHz MAS) unless noted, or a MAS E-free room temperature probe (at 16.4 T, 12 kHz MAS). Each sample contained 3 mg of <sup>15</sup>N/<sup>13</sup>C labeled protein and was packed in a 3.2 mm rotor. **(A, B)** MD simulation snapshot (taken at 301 ns) of Ca<sup>2+</sup>-bound Vn-HX (PDB: 7txr, 7rj9). Colors denote structural repeats HX1 (blue), HX2 (green), HX3 (yellow), and HX4 (red). Spheres denote the four rim-Ala N atoms, and bound ions Ca<sup>2+</sup> (pink), Na<sup>+</sup> (indigo), and Cl<sup>-</sup> (cyan). Sticks denote the four rim-Asp at the top of propeller shaft and the N-and C-terminal Cys (C156 and C472) that circularize the propeller. **(C)** 1D <sup>1</sup>H-<sup>13</sup>C CP spectra. **(D, E)** 2D <sup>13</sup>C/<sup>13</sup>C DARR and <sup>15</sup>N/<sup>13</sup>C NCA spectra obtained with the CryoProbe at 4 °C (black) or 25 °C (red). Yellow crosses mark assigned solution NMR peaks for Ca<sup>2+</sup>-bound Vn-HX (BMRB 50241). Yellow ovals mark solution NMR signals that are highly shifted or missing in the solid-state NMR data. Zoom inset boxes mark examples of broad signals. Dashed boxes mark Lys sidechain signals. The NCA spectra at 4 °C and 25 °C were respectively acquired with RF spectral widths of 3,000 Hz and 2,400 Hz in the t1 dimension, thus the <sup>15</sup>N signals from Arg and Lys sidechains appear in different <sup>15</sup>N spectral regions.

Vn and HAP are two major components of the ectopic deposits that accumulate under the retinal pigment epithelial cell layer in AMD eyes and other degenerative disease settings (Bergen et al., 2019; Ekmekci et al., 2002; Zhang et al., 2004; Shin et al., 2008; Luibl et al., 2006; Mullins et al., 2000). The deposition of Vn with lipids and HAP is a hallmark of AMD, AD and other diseases of aging, but the mechanism for deposit formation and accumulation remains unknown. Atomicresolution structural data is essential for gaining mechanistic insights into the disease process, and solid-state NMR is ideally suited for the task, but its inherently low sensitivity poses a challenge. We show that the enhanced sensitivity afforded by the CryoProbe enabled two and three-dimensional experiments to be acquired for resonance assignments and gaining structural and dynamics insights about the Vn-HAP assembly.

### 1. Results and discussion

# 1.1. The MAS CryoProbe yields high sensitivity data

Recently (Shin et al., 2019, 2020; Tian et al., 2022), we determined the three-dimensional structure of the hemopexin-like (HX) domain of Vn and used NMR to describe its interactions with ionic calcium ( $Ca^{2+}$ ) and mineralized HAP (Ca<sub>10</sub>(PO<sub>4</sub>)<sub>6</sub>(OH)<sub>2</sub>). Vn-HX (Fig. S1) forms a fourbladed  $\beta/\alpha$  propeller where each HX repeat (HX1-HX4) corresponds to one propeller blade ( $\beta 1-\beta 2-\beta 3-\alpha$ ) and the propeller is circularized by a disulfide bond between the terminal C156 and C472 (Fig. 1A, B). The propeller top, defined as the N-terminal end of the  $\beta 1$  strands, forms a smooth surface, while more dynamic loops of variable lengths extend from the bottom, including two flexible regions spanning residues 283-324 and 354-435, which were deleted to facilitate refolding and crystallization. The propeller shaft occludes a NaCl molecule, coordinated by the backbone carbonyl oxygens (Na<sup>+</sup>) and amide hydrogens (Cl $^-$ ) of residues in the shaft-lining  $\beta$ 1 strands (F164, A209, A257, A349), and four Asp residues at the start of β1 (D162, D207, D255, D347) crown the rim of the propeller shaft. The sidechain carboxylate and backbone carbonyl oxygens of these rim-Asp form a Ca<sup>2+</sup> binding site with sufficient affinity to suggest that circulating Vn is Ca<sup>2+</sup>-bound (Shin et al., 2020; Tian et al., 2022).

Solid-state NMR is the method of choice for examining the interaction of Vn with crystalline HAP. Previously, we used solid-state NMR to show that Vn-HX uses its  $Ca^{2+}$  binding site to associate with HAP (Shin et al., 2020). The spectra, acquired with an E-free room temperature MAS probe, yielded useful initial data but were insufficiently sensitive to allow multidimensional data acquisition for resonance assignments and detailed structural studies. To examine the potential of the MAS Cryo-Probe to overcome this sensitivity challenge, we prepared two separate samples, each containing 3 mg of <sup>13</sup>C/<sup>15</sup>N-labeled Vn-HX associated with HAP nanospheres (50 nm diameter) and packed into a 3.2 mm MAS rotor, and acquired one-dimensional CP <sup>13</sup>C spectra using either the MAS CryoProbe at 14.1 T (600 MHz <sup>1</sup>H frequency) or an E-free room temperature MAS probe at 16.4 T (700 MHz <sup>1</sup>H frequency). The resulting spectra (Fig. 1C) demonstrate that, notwithstanding the lower magnetic field strength, the CryoProbe yields a significant signal enhancement factor of  $\sim 3.2$  for  $^{1}H^{-13}C$  cross polarization (CP).

SDS-PAGE analysis of the supernatant obtained after incubating the protein with HAP nanospheres and benchtop centrifugation (5 min; 17,000g) confirms that the NMR signal results from HAP-associated Vn-HX (Shin et al., 2020). Incubation with HAP effectively depletes Vn-HX from solution, while the protein remains in solution after the same centrifugation protocol in the absence of HAP. Moreover, HAP association is completely blocked by the known HAP ligand citrate (Hu et al., 2010), while supplementation with soluble CaCl<sub>2</sub> enhances Vn-HAP association as previously reported for osteocalcin (Hoang et al., 2003; Scudeller et al., 2017). Notably, the <sup>13</sup>C spectra obtained by through-space <sup>1</sup>H-<sup>13</sup>C dipolar CP confirm that association with HAP immobilizes the protein on the microsecond time scale. We conclude therefore

that the NMR signal arises from HAP-associated Vn-HX.

The resulting signal enhancement made it possible to further acquire two-dimensional <sup>13</sup>C/<sup>13</sup>C DARR (dipolar assisted rotational resonance) and  $^{15}\text{N}/^{13}\text{C}$  NCA spectra (Fig. 1D, E) that reveal resolved signals from Ala, Gly, Ile, Ser, Thr and Val spin systems, including low intensity peaks. High quality spectra could be obtained at 4 °C with total acquisition times of 4 h for DARR and 6 h for NCA, or at 25 °C with a total acquisition time of 28 h for NCA. Comparison with the assigned solution NMR spectra of Ca<sup>2+</sup>-bound Vn-HX (BMRB code 50241; acquired at 30  $^{\circ}\text{C})$  shows that several signals are shifted or missing in the solid-state NMR spectra, including those from Gly, Thr, Val and Tyr residues (G191, G267, G328, T325, T329, V188, Y468) in surface-exposed, dynamic regions of the protein. In other cases, signals are broadened or appear as multiple peaks reflecting slow exchange dynamics among multiple conformations. These include signals from I465 at the start of the HX4  $\alpha$ -helix, and T451 in the HX4  $\beta$ 3- $\beta$ 4 loop (Fig. 1E). The data reflect the range of conformational dynamics observed for HAP-associated Vn. Overall, the spectral linewidths are broader at 4 °C than 25 °C, consistent with freezing out of dynamic exchange among multiple conformations.

The enhanced sensitivity of the CryoProbe also allowed us to acquire three-dimensional NCACX and NCOCX solid-state NMR spectra (Fig. S2) in a practical timeframe of approximately 10 days, compared to estimated 100 days that would have been needed to acquire the same data set with a room temperature probe. The resulting data set was used to assign 106 out of 204 expected sets of N, CA, CO, and CB chemical shifts (Table S1). Comparison with the previously assigned solution NMR chemical shifts for Ca<sup>2+</sup>-bound Vn-HX (BMRB: 50241) reveals striking similarity (Fig. S3A), even though the data sets were acquired at different temperatures of 4  $^{\circ}\text{C}$  for solid-state NMR and 30  $^{\circ}\text{C}$  for solution NMR. The chemical shift differences are in the range of 2 ppm, further indicating that the overall structure of Vn-HX is maintained in both the immobilized HAP-bound state and soluble Ca<sup>2+</sup>-bound state. Further comparison of the assigned chemical shifts with their random coil values provides an index of protein secondary structure (Wishart and Sykes, 1994). In both Ca<sup>2+</sup>-bound and HAP-bound Vn-HX, the analysis is consistent with the known three-dimensional structure of the protein, with <sup>13</sup>CA and <sup>13</sup>CO signals shifted downfield and <sup>15</sup>N signals shifted upfield for  $\beta$ -strands and the converse for  $\alpha$ -helices (Fig. S3B). The data, therefore, indicate that the fundamental four-bladed propeller structure remains unchanged in the solid-state regime upon co-sedimentation

Notably, four rim-Ala (A163, A208, A256, A348), that line the propeller shaft one level below the Ca<sup>2+</sup>-binding rim-Asp, have very similar  $^{15}$ N chemical shifts in the spectra of the HAP-bound and Ca $^{2+}$ -bound protein. Previously, we showed that these signals are highly sensitive to metal ion coordination and undergo a downfield shift of approximately 5 ppm from the Na<sup>+</sup>-bound to the Ca<sup>2+</sup>-bound protein (Shin et al., 2020). The data therefore demonstrate that Vn utilizes the same coordination site to associate with both freely soluble Ca<sup>2+</sup> and HAP. Marked similarities notwithstanding, notable differences between the two data sets are observed for several signals, particularly from sites at the top of the propeller channel in the periphery of the four rim-Asp (Fig. S3A). These differences may reflect variable susceptibility of surface-exposed protein sites to temperature, and to the mineral HAP versus soluble Ca<sup>2+</sup> environments, but it is also possible that they reflect new interactions with water and HAP phosphate and hydroxide groups, which are predicted to play a role in mediating protein-HAP association and protein-mediated HAP mineralization. Resonance assignments enabled by the MAS CryoProbe provide an avenue for addressing these important mechanistic questions.

# 1.2. Protein dynamics

The three-dimensional NCACX and NCOCX data from the CryoProbe show that the side chain carboxylate groups of the four rim-Asp residues

yield high-intensity, inter-residue  $CO_i-CG_{i+1}$  signals (Fig. 2A), consistent with their high conformational order at the propeller surface. This order appears to extend to the neighboring  $\beta 2$ - $\beta 3$  turns (Fig. 2B), in line with the crystal structures and predictions from molecular dynamics (MD) simulations (Tian et al., 2022) that the amide N atoms of the Gly residues at the apex of the four  $\beta 2$ - $\beta 3$  turns (G177, G224, G276, G441) form polar contacts with the rim-Asp sidechain carboxylates (Fig. 2C). By contrast, the NCA and NCB planes from the three-dimensional data set show that residues D166, A174 and I243 each yield two sets of signals, consistent with the presence of two conformational states (Fig. S4).

Overall, the solid-state NMR data reflect a wide range of dynamics for different regions of the protein.

We performed additional experiments to further probe protein dynamics. Protein sites with dynamics faster than the nanosecond time scale cannot be detected by dipolar-based CP experiments because the fast molecular motions average out anisotropic spin interactions. Fast dynamics, however, also increase T2 relaxation times, enabling throughbond INEPT experiments based on through-bond, J-coupling transfer to be used. The high sensitivity of the MAS CryoProbe allowed us to acquire one and two-dimensional INEPT-HETCOR spectra at 25 °C that reveal

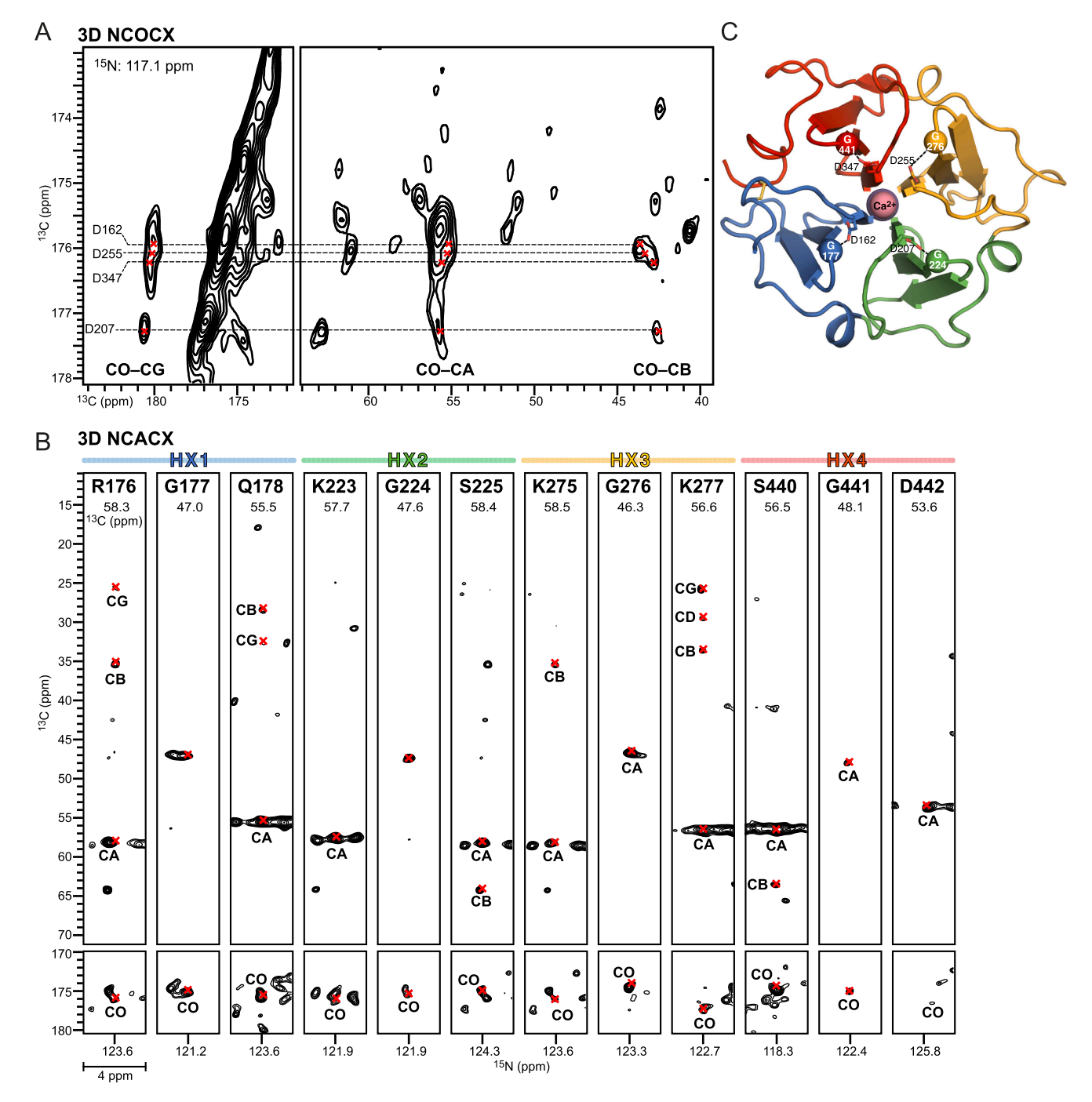


Fig. 2. Solid-state NMR NCOCX and NCACX spectra acquired with the MAS CryoProbe. (A) 2D plane extracted from 3D NCOCX spectrum showing intramolecular CO-CG, COCA and CO-CB correlations from rim-Asp residues. (B) 2D strips extracted from 3D NCACX spectrum showing intra-residue N-CA, N-CB, and N-CO correlations from the  $\beta$ 2-  $\beta$ 3 turns for the four HX repeats lining the channel. Red crosses mark assigned peaks. The strips were plotted at a contour level set to 7.0 times the estimated noise level. (C) MD simulation snapshot (taken at 301 ns) of Ca<sup>2+</sup>-bound Vn-HX showing polar contacts (dashed lines) between Gly amide N atoms (sphere) and the rim-Asp carboxylates (stick).

the presence of fast dynamics sites (Fig. 3A, B), with several HA-CA and HB-CB correlation peaks mapping to solution NMR signals predicted by MD to undergo rapid nanosecond fluctuations (Fig. 3C), as in the  $\beta 3-\alpha$  regions of the HX1 and HX3 repeats (A187, V188, G191, Q285, A327, T329) (Tian et al., 2022). The CryoProbe clearly provides sufficient signal enhancement to enable these types of experiments for complex multi-component samples, and the resulting data provide a starting point for the assignment of solid-state NMR INEPT spectra using NOESY and TOBSY sequences.

# 1.3. Detection of protein-water interactions

Water-edited solid-state NMR experiments can provide valuable insights into protein-water interactions for a range of complex samples (Williams and Hong, 2014). In these experiments, polarization is driven from water molecules to protein sites via mechanisms that include chemical exchange, NOE, and spin diffusion. Using the room temperature E-free MAS probe at 16.4 T, we acquired one-dimensional water-edited  $^{15}{\rm N}$  CP spectra of HAP-bound Vn-HX (Fig. S5A). As expected, longer mixing times increase signal intensity due to  $^{1}{\rm H}$  spin diffusion but this mechanism of polarization transfer is non-specific. Residue-specific water-protein interactions may be detected with shorter mixing times but the signals are less intense and hence more challenging to detect. The 2D water-edited  $^{1}{\rm H}/^{15}{\rm N}$  CP spectrum acquired with a 2 ms  $T_2$  filter and 10 ms of  $^{1}{\rm H}-^{1}{\rm H}$  mixing demonstrates water accessibility to specific  $^{15}{\rm N}$  sites in the protein backbone and Arg and Lys side chains (Fig. S5B).

Using the MAS CryoProbe we then acquired a two-dimensional water-edited NCA spectrum with 10 ms  $^1H^{-1}H$  mixing at 25  $^{\circ}C$ 

(Fig. 4A). Water-polarization gives rise to many NCA signals, including those from sites involved in (A208, A256, A348) or peripheral to (G177, G224, G276, and G441) the Ca<sup>2+</sup> binding site. As expected, the bulk of water-edited signal intensity maps to the surface of the threedimensional protein structure, while signals from sites in the protein core are either missing or very weak (Fig. 4B). The data are in line with predictions from MD simulations (Fig. 4C). There are, however, notable exceptions of low intensity signals arising from surface-exposed residues, including T165, D166, A174, I243, L235, and V234. Interestingly, MD simulations of Ca<sup>2+</sup>bound Vn-HX predict low water-accessibility for these sites, and in the case of T165 and D166, this effect was attributed to occlusion of the bottom of the propeller channel upon Ca<sup>2+</sup> coordination at the top, with the net effect of reducing water accessibility into the cavity. Previously, we proposed that such subtle conformational changes and resulting alteration of the water accessibility profile are responsible for the capacity of Vn to adapt to its environment and sustain excursions in shear stress and temperature encountered in the circulation. The water-edited data provide the first experimental confirmation of this effect.

# 2. Conclusions

Sensitivity is a major bottleneck of biomolecular NMR and poses a particular challenge for solid-state NMR studies of complex biological systems. Here we have shown that the new MAS CryoProbe provides highly enhanced signal over noise, enabling multi-dimensional solid-state NMR experiments to be successfully performed for resonance assignment, dynamics analysis, and water accessibility studies of the

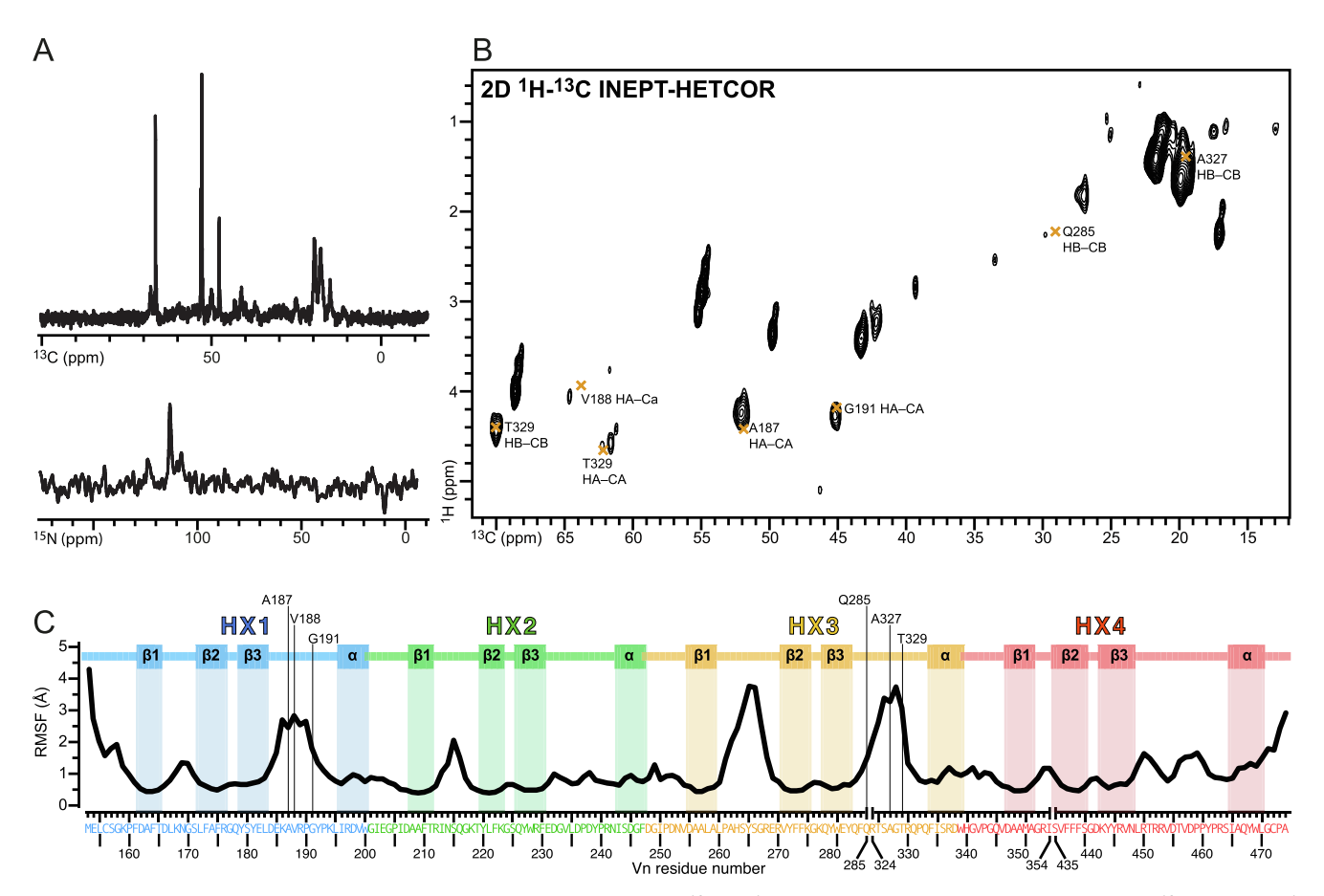


Fig. 3. Solid-state NMR INEPT spectra acquired with the MAS CryoProbe. (A)  $10^{13}$ C and  $^{15}$ N refocused INEPT spectra acquired with 2,000 ( $^{13}$ C) and 5,000 ( $^{15}$ N) scans, at 25 °C. (B)  $20^{1}$ H $^{-13}$ C INEPT-HETCOR spectrum acquired in 6 h, at 25 °C. Yellow crosses represent solution NMR assignments of selected signals that match with the solid-state NMR data and correspond to dynamic sites of Vn. (C) Time-averaged root mean square fluctuations (RMSF) of Vn-HX. The trace is the average, calculated for heavy atoms, over the last 500 ns of five independent 1  $\mu$ s MD simulations performed at 30 °C for Ca $^{2+}$ -bound Vn-HX. Structural elements of the HX1-HX4 propeller blades are depicted above the data. Vertical lines mark protein sites identified to undergo nanosecond dynamics in the INPET NMR spectra.

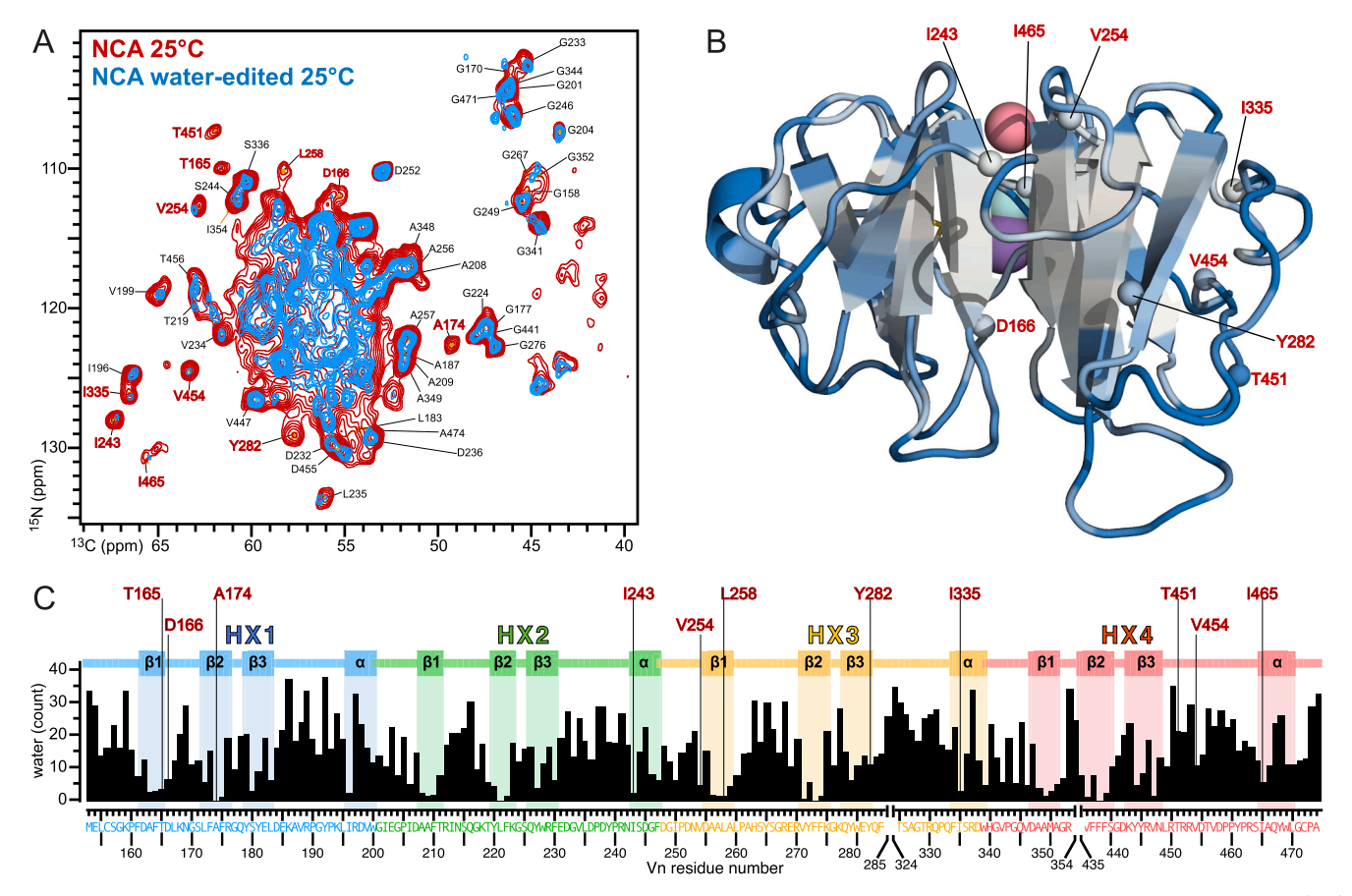


Fig. 4. Water-edited solid-state NMR spectra acquired with the MAS CryoProbe. (A) 2D NCA (red) and water-edited NCA (blue) acquired with 10 ms  $^{1}H^{-1}H$  mixing time. Red labels mark peaks with no or little signal from water polarization. (B) MD simulation snapshot (taken at 301 ns) of  $Ca^{2+}$ -bound Vn-HX. Color reflects the number of water molecules within 5 Å of a protein site, from white (0 water) to blue (4 waters), determined from MD simulations as in (C). Spheres represent  $Ca^{2+}$  (pink),  $Cl^-$  (cyan) and  $Na^+$  (indigo). Small white-blue spheres represent CA atoms of sites with no or little signal from water polarization in the water-edited NCA spectrum. (C) MD time-averaged number of water molecules within 5 Å of each residue of Vn-HX. Each bar represents the average, calculated for heavy atoms, over the last 500 ns of five independent 1  $\mu$ s MD simulations performed at 30 °C for  $Ca^{2+}$ -bound Vn-HX. Structural elements of the HX1-HX4 propeller blades are depicted above the data. Vertical lines and red labels mark sites with no or little signal from water polarization in panel (A).

blood protein Vn associated with HAP. The data reveal structural and dynamic features of the protein-HAP complex that could not have been discerned with a room temperature probe operating at ambient temperature. The ability to correlate MD-based predictions with experimental data is particularly exciting, as the water-edited data provide new experimental insights into the role of water in modulating the environmental adaptation of Vn. The MAS CryoProbe dramatically broadens the range of biomolecular systems that can be examined with solid-state NMR to include complex multi-component assemblies.

# 3. Materials and methods

# 3.1. Sample preparation

Vn-HX was prepared from *E. coli* as described (Shin et al., 2019). Briefly, uniformly  $^{15}$ N/ $^{13}$ C labeled protein was prepared by growing bacteria on minimal M9 medium containing ( $^{15}$ NH<sub>4</sub>)<sub>2</sub>SO<sub>4</sub> and  $^{13}$ C-glucose (Cambridge Isotopes). HAP-associated Vn-HX was prepared by gently mixing 28 mg of protein in 1.2 mL buffer (20 mM MES, pH 6.5, 300 mM NaCl) with 200 mg of HAP nano-powder (50 nm diameter; Sigma-Aldrich cat. 900194). After removing the supernatant by bench-top centrifugation (5 min; 17,000 x g) and washing the Vn-loaded HAP with buffer (20 mM MES pH 6.5), the sample was transferred into the MAS rotor for NMR. Two identical samples were prepared and loaded into separate 3.2 mm rotors for NMR studies with either the CryoProbe or the room temperature probe.

# 3.2. Solid state NMR experiments

Solid-state NMR experiments were performed on a 14.1 T Bruker spectrometer, equipped with a NEO console and a 3.2 mm  $^1 H/^{13} C/^{15} N$  MAS CryoProbe, or on a 16.4 T Bruker spectrometer, equipped with a NEO console and a 3.2 mm  $^1 H/^{13} C/^{15} N$  E-free MAS probe with the RF components operating at room temperature. Experiments were acquired at sample temperatures of 4 °C or 25 °C, with a spinning frequency of 12 kHz and 20 or 30 ms of acquisition time. Recycle delays were 2 sec for one and two-dimensional experiments, and 1.2 sec for three-dimensional experiments. All CP-based experiments were acquired with 83 kHz SPINAL-64  $^1 H$  decoupling (Fung et al., 2000), whereas 5–10 kHz swTPPM  $^1 H$  decoupling (Vinod Chandran et al., 2008) was used for the INEPT experiments.

The  $\pi/2$  pulse lengths were 2.5  $\mu$ s for  $^{1}$ H, 6  $\mu$ s for  $^{13}$ C and  $^{15}$ N. Conditions for HC and HN CP were optimized using a  $^{1}$ H tangential ramp with contact time set to 1 ms (Hartmann and Hahn, 1962), while NCA and NCO SPECIFIC-CP transfer was optimized with a  $^{13}$ C tangential ramp and 4 ms contact time (Baldus et al., 1998). For the NCA and NCO transfers, 100 kHz of  $^{1}$ H continuous wave decoupling was applied, and  $^{13}$ C and  $^{15}$ N RF amplitudes were respectively set to 53.0 kHz and 46.2 kHz for NCA, and 42.7 kHz and 16.0 kHz for NCO.

The two-dimensional CXCX spectrum was acquired with 16 transients, 20 ms  $^{13}$ C $^{-13}$ C DARR mixing, 28  $\mu$ s t1 dwell time, and 178 t1 increments, for a total experimental time of approximately 4 h (Takegoshi, 2001). The 2D NCA spectra were respectively acquired at 4 °C,

with a t1 dwell time of 333  $\mu$ s, 40 t1 increments, and 128 transients ( $\sim$ 6 h), or 25  $^{\circ}$ C with a t1 dwell time of 417  $\mu$ s, 32 t1 increments, and 768 transients( $\sim$ 28 h).

The 2D water-edited NCA experiments (Ader et al., 2009) were acquired at 25 °C, with a t1 dwell time of 417  $\mu$ s, 32 increments, 2048 transients, a 2 ms T2-filter, and 10 ms of  $^{1}H_{-}^{1}H$  mixing ( $\sim$ 73 h).

For  $^{13}\text{C}$  INEPT experiments, two polarization transfer delays were set to 1/(4\*J) and 1/(6\*J), respectively corresponding to 1.66 ms and 1.11 ms, optimized for 150 Hz HC J-coupling (Andronesi et al., 2005). For  $^{15}\text{N}$  INEPT experiment, two polarization transfer delays were set to 2.72 ms and 1.81 ms, optimized for 92 Hz HN J-coupling. 2D  $^{1}\text{H}/^{13}\text{C}$  INEPT-HETCOR was acquired with a t1 dwell time of 83  $\mu\text{s}$ , 40 increments, and 128 transients (~6 h).

Each of the three-dimensional NCACX and NCOCX data sets was acquired with 50 ms of CORD mixing time, 96 transients, 19 t1 ( $^{15}$ N) and 48 t2 (CA or CO) points with respective dwell times of 333  $\mu$ s and 166  $\mu$ s ( $\sim$ 4.8 days) (Hou et al., 2013; Castellani et al., 2002). The room temperature MAS probe was used to acquire water-edited 1D and 2D  $^{1}$ H/ $^{15}$ N-CP spectra with  $^{1}$ H t1 dwell time and increments set to 240  $\mu$ s and 32 real t1 increments. A total of 2048 and 384 transients were acquired for the 1D and 2D spectra, respectively, with 2 ms T2-filter. In the 2D experiment, the  $^{1}$ H dimension was t1 evolved after the T2 filter, followed by 10 ms of  $^{1}$ H- $^{1}$ H mixing,  $^{1}$ H- $^{15}$ N CP, and  $^{15}$ N detection (Williams and Hong, 2014). All multi-dimensional experiments were acquired using States-TPPI acquisition mode.

Spectra were processed with NMRpipe and analyzed using Poky (Sparky) software (Delaglio et al., 1995; Lee et al., 2021). The threedimensional data were processed using SMILE linear prediction to twice the number of real data points in both the t1 and t2 dimensions (Ying et al., 2017). 2D DARR, NCA, and CP spectra were processed with Lorentz-to-Gauss (GM) window functions with (g1, g2) values set to (30, 60) in the t2 dimension. The t1 dimensions were processed with a  $60^{\circ}$ sine-squared bell window function. 2D <sup>1</sup>H/<sup>13</sup>C INEPT-HETCOR spectra were processed with a cosine-squared bell window function in both dimensions. 3D spectra were processed with Lorentz-to-Gauss (GM) window functions, with (g1, g2) values of (15, 45), (25, 75), and (30, 55) for t1, t2, and t3 dimensions respectively. The 3D strip plots were plotted using Python modules nmrglue, numpy and matplotlib (Helmus and Jaroniec, 2013), whereas all the other 1D and 2D spectra were plotted using NMRpipe and Sparky. For 2D and 3D figures, the lowest contour threshold was set to at least 4.5 times the estimated noise, the number of contours levels and scale factors were in the range of 30-40 and 1.1-1.4 respectively.

# 3.3. MD simulations

All-atom MD simulations were described previously (Tian et al., 2022). Five independent 1  $\mu s$  MD simulations were performed using the CHARMM36m force fields (Brooks et al., 2009) with the TIP3P water model (Jorgensen et al., 1983), the temperature set to 303.15 K for simulations at 30 °C, and the pressure maintained at 1 bar. The five independent systems for MD were identical to the experimental protein sequence. MD production simulations were conducted with OpenMM (Eastman et al., 2013) for 1  $\mu s$ , and the last 500 ns of trajectories were used for analysis. For each simulation, trajectories were generated every 1 ns, and trajectories from all simulations were combined for analysis in each system. Statistical analyses were performed with in-house Python scripts using MDAnalysis and JupyterNotebook.

# CRediT authorship contribution statement

**T. Gopinath:** . **Kyungsoo Shin:** Writing – review & editing, Writing – original draft, Formal analysis, Data curation. **Ye Tian:** Formal analysis, Data curation. **Wonpil Im:** Formal analysis. **Jochem Struppe:** Methodology, Investigation, Formal analysis. **Barbara Perrone:** Methodology, Investigation, Formal analysis. **Alia Hassan:** Methodology,

Investigation, Formal analysis. Francesca M. Marassi: Writing – review & editing, Writing – original draft, Visualization, Investigation, Funding acquisition, Formal analysis, Conceptualization.

# Declaration of competing interest

The authors declare that they have no known competing financial interests or personal relationships that could have appeared to influence the work reported in this paper.

# Data availability

Data will be made available on request.

# Acknowledgements

This study was supported by grants from the National Institutes of Health (GM 118186) and the National Science Foundation (MCB 2111728), and by Bruker Biospin.

# Appendix A. Supplementary material

Supplementary material to this article can be found online at htt ps://doi.org/10.1016/j.jsb.2024.108061.

## References

- Ader, C., Schneider, R., Seidel, K., Etzkorn, M., Becker, S., Baldus, M., 2009. Structural rearrangements of membrane proteins probed by water-edited solid-state NMR spectroscopy. J. Am. Chem. Soc. 131, 170–176.
- Andreas, L.B., Jaudzems, K., Stanek, J., Lalli, D., Bertarello, A., Le Marchand, T., Cala-De Paepe, D., Kotelovica, S., Akopjana, I., Knott, B., et al., 2016. Structure of fully protonated proteins by proton-detected magic-angle spinning NMR. PNAS 113, 9187–9192.
- Andronesi, O.C., Becker, S., Seidel, K., Heise, H., Young, H.S., Baldus, M., 2005. Determination of membrane protein structure and dynamics by magic-angle-spinning solid-state NMR spectroscopy. J. Am. Chem. Soc. 127, 12965–12974.
- Anon., 2022. Alzheimer's disease facts and figures. Alzheimers Dement. 18, 700–789.
   Baldus, M., Petkova, A.T., Herzfeld, J., Griffin, R.G., 1998. Cross polarization in the tilted frame: assignment and spectral simplification in heteronuclear spin systems. Mol. Phys. 95, 1197–1207.
- Bergen, A.A., Arya, S., Koster, C., Pilgrim, M.G., Wiatrek-Moumoulidis, D., van der Spek, P.J., Hauck, S.M., Boon, C.J.F., Emri, E., Stewart, A.J., et al., 2019. On the origin of proteins in human drusen: The meet, greet and stick hypothesis. Prog. Retin. Eye Res. 70, 55–84.
- Bertazzo, S., Gentleman, E., Cloyd, K.L., Chester, A.H., Yacoub, M.H., Stevens, M.M., 2013. Nano-analytical electron microscopy reveals fundamental insights into human cardiovascular tissue calcification. Nat. Mater. 12, 576–583.
- Biedenbander, T., Aladin, V., Saeidpour, S., Corzilius, B., 2022. Dynamic nuclear polarization for sensitivity enhancement in biomolecular solid-state NMR. Chem. Rev. 122, 9738–9794.
- Brooks, B.R., Brooks 3rd, C.L., Mackerell Jr., A.D., Nilsson, L., Petrella, R.J., Roux, B., Won, Y., Archontis, G., Bartels, C., Boresch, S., et al., 2009. CHARMM: the biomolecular simulation program. J. Comput. Chem. 30, 1545–1614.
- Callon, M., Malar, A.A., Pfister, S., Rimal, V., Weber, M.E., Wiegand, T., Zehnder, J., Chavez, M., Cadalbert, R., Deb, R., et al., 2021. Biomolecular solid-state NMR spectroscopy at 1200 MHz: the gain in resolution. J. Biomol. NMR 75, 255–272.
- Castellani, F., van Rossum, B., Diehl, A., Schubert, M., Rehbein, K., Oschkinat, H., 2002. Structure of a protein determined by solid-state magic-angle-spinning NMR spectroscopy. Nature 420, 98–102.
- Chow, W.Y., De Paepe, G., Hediger, S., 2022. Biomolecular and biological applications of solid-state NMR with dynamic nuclear polarization enhancement. Chem. Rev. 122, 9795–9847.
- Delaglio, F., Grzesiek, S., Vuister, G.W., Zhu, G., Pfeifer, J., Bax, A., 1995. NMRPipe: a multidimensional spectral processing system based on UNIX pipes. J. Biomol. NMR 6, 277–293.
- Du, Y., Struppe, J., Perrone, B., Hassan, A., Codina, A., Su, Y., 2023. Efficient analysis of pharmaceutical drug substances and products using a solid-state NMR CryoProbe. Analyst 148, 724–734.
- Eastman, P., Friedrichs, M.S., Chodera, J.D., Radmer, R.J., Bruns, C.M., Ku, J.P., Beauchamp, K.A., Lane, T.J., Wang, L.P., Shukla, D., et al., 2013. OpenMM 4: A reusable, extensible, hardware independent library for high performance molecular simulation. J. Chem. Theory Comput. 9, 461–469.
- Ekmekci, H., Sonmez, H., Ekmekci, O.B., Ozturk, Z., Domanic, N., Kokoglu, E., 2002.
  Plasma vitronectin levels in patients with coronary atherosclerosis are increased and correlate with extent of disease. J. Thromb. Thrombolysis 14, 221–225.

- Frederick, K.K., Michaelis, V.K., Corzilius, B., Ong, T.C., Jacavone, A.C., Griffin, R.G., Lindquist, S., 2015. Sensitivity-enhanced NMR reveals alterations in protein structure by cellular milieus. Cell 163, 620–628.
- Friedman, D.S., O'Colmain, B.J., Munoz, B., Tomany, S.C., McCarty, C., de Jong, P.T., Nemesure, B., Mitchell, P., Kempen, J., 2004. Eye Diseases Prevalence Research G: Prevalence of age-related macular degeneration in the United States. Arch. Obhthalmol. 122, 564–572.
- Fung, B.M., Khitrin, A.K., Ermolaev, K., 2000. An improved broadband decoupling sequence for liquid crystals and solids. J. Magn. Reson. 142, 97–101.
- Gallardo, R., Ranson, N.A., Radford, S.E., 2020. Amyloid structures: much more than just a cross-β fold. Curr. Opin. Struct. Biol. 60, 7–16.
- Gan, Z., Hung, I., Wang, X., Paulino, J., Wu, G., Litvak, I.M., Gor'kov, P.L., Brey, W.W., Lendi, P., Schiano, J.L., et al., 2017. NMR spectroscopy up to 35.2T using a seriesconnected hybrid magnet. J. Magn. Reson. 284, 125–136.
- Gibbs, E., Perrone, B., Hassan, A., Kummerle, R., Kriwacki, R., 2020. NPM1 exhibits structural and dynamic heterogeneity upon phase separation with the p14ARF tumor suppressor. J. Magn. Reson. 310, 106646.
- Gopinath, T., Weber, D.K., Veglia, G., 2020. Multi-receiver solid-state NMR using polarization optimized experiments (POE) at ultrafast magic angle spinning. J. Biomol. NMR 74, 267–285.
- Gor'kov, P.L., Chekmenev, E.Y., Li, C., Cotten, M., Buffy, J.J., Traaseth, N.J., Veglia, G., Brey, W.W., 2007. Using low-E resonators to reduce RF heating in biological samples for static solid-state NMR up to 900 MHz. J. Magn. Reson. 185, 77–93.
- Grant, C.V., Wu, C.H., Opella, S.J., 2010. Probes for high field solid-state NMR of lossy biological samples. J. Magn. Reson. 204, 180–188.
- Hartmann, S.R., Hahn, E.L., 1962. Nuclear double resonance in the rotating frame. Phys. Rev. 128, 2042–2053.
- Hassan, A., Quinn, C.M., Struppe, J., Sergeyev, I.V., Zhang, C., Guo, C., Runge, B., Theint, T., Dao, H.H., Jaroniec, C.P., et al., 2020. Sensitivity boosts by the CPMAS CryoProbe for challenging biological assemblies. J. Magn. Reson. 311, 106680.
- Helmus, J.J., Jaroniec, C.P., 2013. Nmrglue: an open source Python package for the analysis of multidimensional NMR data. J. Biomol. NMR 55, 355–367.
- Hoang, Q.Q., Sicheri, F., Howard, A.J., Yang, D.S., 2003. Bone recognition mechanism of porcine osteocalcin from crystal structure. Nature 425, 977–980.
- Holmes, J.B., Liu, V., Caulkins, B.G., Hilario, E., Ghosh, R.K., Drago, V.N., Young, R.P., Romero, J.A., Gill, A.D., Bogie, P.M., et al., 2022. Imaging active site chemistry and protonation states: NMR crystallography of the tryptophan synthase alphaaminoacrylate intermediate. PNAS 119.
- Hou, G., Yan, S., Trébosc, J., Amoureux, J.-P., Polenova, T., 2013. Broadband homonuclear correlation spectroscopy driven by combined R2nv sequences under fast magic angle spinning for NMR structural analysis of organic and biological solids. J. Magn. Reson. 232, 18–30.
- Hu, Y.Y., Rawal, A., Schmidt-Rohr, K., 2010. Strongly bound citrate stabilizes the apatite nanocrystals in bone. PNAS 107, 22425–22429.
- Hurd, M.D., Martorell, P., Delavande, A., Mullen, K.J., Langa, K.M., 2013. Monetary costs of dementia in the United States. N. Engl. J. Med. 368, 1326–1334.
- Jaudzems, K., Polenova, T., Pintacuda, G., Oschkinat, H., Lesage, A., 2019. DNP NMR of biomolecular assemblies. J. Struct. Biol. 206, 90–98.
- Jorgensen, W.L., Chandrasekhar, J., Madura, J.D., Impey, R.W., Klein, M.L., 1983. Comparison of simple potential functions for simulating liquid water. J. Chem. Phys. 79, 926–935.
- Kaplan, M., Narasimhan, S., de Heus, C., Mance, D., van Doorn, S., Houben, K., Popov-Celeketic, D., Damman, R., Katrukha, E.A., Jain, P., et al., 2016. EGFR dynamics change during activation in native membranes as revealed by NMR. Cell 167 (1241–1251), e1211.
- Kent, J.E., Fujimoto, L.M., Shin, K., Singh, C., Yao, Y., Park, S.H., Opella, S.J., Plano, G. V., Marassi, F.M., 2021. Correlating the structure and activity of *Y. pestis* Ail in a bacterial cell envelope. Biophys. J. 120, 453–462.
- Lee, W., Rahimi, M., Lee, Y., Chiu, A., 2021. POKY: a software suite for multidimensional NMR and 3D structure calculation of biomolecules. Bioinformatics 37, 3041–3042.
- Luchinat, E., Cremonini, M., Banci, L., 2022. Radio signals from live cells: the coming of age of in-cell solution NMR. Chem. Rev. 122, 9267–9306.
- Luibl, V., Isas, J.M., Kayed, R., Glabe, C.G., Langen, R., Chen, J., 2006. Drusen deposits associated with aging and age-related macular degeneration contain nonfibrillar amyloid oligomers. J. Clin. Invest. 116, 378–385.

- Mullins, R.F., Russell, S.R., Anderson, D.H., Hageman, G.S., 2000. Drusen associated with aging and age-related macular degeneration contain proteins common to extracellular deposits associated with atherosclerosis, elastosis, amyloidosis, and dense deposit disease. FASEB J. 14, 835–846.
- Penzel, S., Oss, A., Org, M.L., Samoson, A., Bockmann, A., Ernst, M., Meier, B.H., 2019. Spinning faster: protein NMR at MAS frequencies up to 126 kHz. J. Biomol. NMR 73, 19–29
- Scudeller, L.A., Srinivasan, S., Rossi, A.M., Stayton, P.S., Drobny, G.P., Castner, D.G., 2017. Orientation and conformation of osteocalcin adsorbed onto calcium phosphate and silica surfaces. Biointerphases 12, 02D411.
- Shin, T.M., Isas, J.M., Hsieh, C.L., Kayed, R., Glabe, C.G., Langen, R., Chen, J., 2008. Formation of soluble amyloid oligomers and amyloid fibrils by the multifunctional protein vitronectin. Mol. Neurodegener. 3, 16.
- Shin, K., Lechtenberg, B.C., Fujimoto, L.M., Yao, Y., Bartra, S.S., Plano, G.V., Marassi, F. M., 2019. Structure of human Vitronectin C-terminal domain and interaction with Yersinia pestis outer membrane protein Ail. Sci. Adv. 5, eaax5068.
- Shin, K., Kent, J.E., Singh, C., Fujimoto, L.M., Yu, J., Tian, Y., Im, W., Marassi, F.M., 2020. Calcium and hydroxyapatite binding site of human vitronectin provides insights to abnormal deposit formation. PNAS 117, 18504–18510.
- Takahashi, H., Ayala, I., Bardet, M., De Paepe, G., Simorre, J.P., Hediger, S., 2013. Solid-state NMR on bacterial cells: selective cell wall signal enhancement and resolution improvement using dynamic nuclear polarization. J. Am. Chem. Soc. 135, 5105–5110
- Takegoshi, K.N., 2001. S; and Terao, T: 13C–1H dipolar-assisted rotational resonance in magic-angle spinning NMR. Chem. Phys. Lett. 344, 631–637.
- Tan, A.C.S., Pilgrim, M.G., Fearn, S., Bertazzo, S., Tsolaki, E., Morrell, A.P., Li, M., Messinger, J.D., Dolz-Marco, R., Lei, J., et al., 2018. Calcified nodules in retinal drusen are associated with disease progression in age-related macular degeneration. Sci. Transl. Med. 10.
- Theillet, F.X., 2022. In-cell structural biology by NMR: The benefits of the atomic scale. Chem. Rev. 122, 9497–9570.
- Thompson, R.B., Reffatto, V., Bundy, J.G., Kortvely, E., Flinn, J.M., Lanzirotti, A., Jones, E.A., McPhail, D.S., Fearn, S., Boldt, K., et al., 2015. Identification of hydroxyapatite spherules provides new insight into subretinal pigment epithelial deposit formation in the aging eye. PNAS 112, 1565–1570.
- Tian, Y., Shin, K., Aleshin, A.E., Im, W., Marassi, F.M., 2022. Calcium-induced environmental adaptability of the blood protein vitronectin. Biophys. J. 121, 3896–3906.
- Tsolaki, E., Doran, W., Overbeck, J., Magnani, L., Olivo, A., Herrmann, I.K., Bertazzo, S., 2021. Nano-analytical characterization of breast tissue biopsies reveals an association between spherical nano and micro particles and invasive malignant breast tumours. bioRxiv. https://doi.org/10.1101/2020.04.29.067660: 2020.2004.2029.067660
- Tsolaki, E., Csincsik, L., Xue, J., Lengyel, I., Bertazzo, S., 2022. Nuclear and cellular, micro and nano calcification in Alzheimer's disease patients and correlation to phosphorylated Tau. Acta Biomater. 143, 138–144.
- phosphorylated Tau. Acta Biomater. 143, 138–144.

  Tycko, R., 2016. Molecular structure of aggregated amyloid-beta: insights from solid-
- state nuclear magnetic resonance. Cold Spring Harb. Perspect. Med. 6. van Leeuwen, R., Klaver, C.C., Vingerling, J.R., Hofman, A., de Jong, P.T., 2003. Epidemiology of age-related maculopathy: a review. Eur. J. Epidemiol. 18, 845–854.
- Vinod Chandran, C., Madhu, P.K., Kurur, N.D., Brauniger, T., 2008. Swept-frequency two-pulse phase modulation (SWf-TPPM) sequences with linear sweep profile for heteronuclear decoupling in solid-state NMR. Magn. Reson. Chem. 46, 943–947.
- Williams, J.K., Hong, M., 2014. Probing membrane protein structure using water polarization transfer solid-state NMR. J. Magn. Reson. 247, 118–127.
- Wishart, D.S., Sykes, B.D., 1994. Chemical shifts as a tool for structure determination Methods Enzymol. 239, 363–392.
- Ying, J., Delaglio, F., Torchia, D.A., Bax, A., 2017. Sparse multidimensional iterative lineshape-enhanced (SMILE) reconstruction of both non-uniformly sampled and conventional NMR data. J. Biomol. NMR 68, 101–118.
- Zhang, R., Barker, L., Pinchev, D., Marshall, J., Rasamoelisolo, M., Smith, C., Kupchak, P., Kireeva, I., Ingratta, L., Jackowski, G., 2004. Mining biomarkers in human sera using proteomic tools. Proteomics 4, 244–256.